h-$ErMnO_3$ absorbance, reflectivity, and emissivity in the terahertz to mid-infrared from 2 to 1700 K: Carrier screening, Fröhlich resonance, small polarons, and bipolarons

Néstor E. Massa,[1,*] Leire del Campo,[2] Karsten Holldack,[3] Aurélien Canizarès,[2] Vinh Ta Phuoc,[4] Paula Kayser,[5] and José Antonio Alonso[6]

[1]*Centro CEQUINOR, Consejo Nacional de Investigaciones Científicas y Técnicas, Universidad Nacional de La Plata, Blvd. 120 1465, B1904 La Plata, Argentina*

[2]*Centre National de la Recherche Scientifique, CEMHTI UPR3079, Université Orléans, F-45071 Orléans, France*

[3]*Helmholtz-Zentrum für Materialien und Energie GmbH, Albert Einstein Strasse 15, D-12489 Berlin, Germany*

[4]*Groupement de Recherche Matériaux Microélectronique Acoustique Nanotechnologies-Université François Rabelais Tours, Faculté des Sciences & Techniques, F- 37200 Tours, France*

[5]*Centre for Science at Extreme Conditions and School of Chemistry, University of Edinburgh, Kings Buildings, Mayfield Road, EH9 3FD Edinburgh, United Kingdom*

[6]*Instituto de Ciencia de Materiales de Madrid, CSIC, Cantoblanco, E-28049 Madrid, Spain*

(Received 28 February 2020; revised 14 July 2020; accepted 2 September 2020; published 12 October 2020)

We report the temperature-dependent THz to mid-infrared response of hexagonal-$ErMnO_3$ using absorption, reflectivity, and emissivity techniques from 2 to 1700 K. At low temperatures, lowest frequency vibrational modes, which extend up the lock-in ferroelectric temperature, coexist with paramagnon excitations and are associated with well-defined crystal-field rare-earth pure magnetic replicas in an intriguing phonon-magnetic convergence enhancing the multiferroic character of *h*-$ErMnO_3$. Increasing the temperature, a number of vibrational bands close to the space group predicted undergo profile broadening and softening. In particular, a distinctive set of bands in the 288–329-cm^{-1} (300 K) range has a component whose profile is carrier screened becoming nearly fully blurred in the intermediate phase between ∼830 and ∼1500 K. Below $T_C \sim 830$ K this asymmetric band, having one component still partially screened, further splits as spin phonon interaction and the tripling of the unit cell take place revealing at $T_N \sim 79$ K a delicate balance of long- and short-range interactions. Ambient Raman scattering brings up evidence of a Fröhlich resonance due to Coulomb interactions between carriers and the macroscopic field linked to the corresponding longitudinal optical-phonon mode. We found it is dynamically correlated to the hexagonal *c*-axis negative thermal expansion. Quantitative analyses of the mid-infrared (MIR) optical conductivity show that it also plays a role in small polarons and mediates in high-temperature bipolarones. Bipolaron profiles at high temperatures change as the sample opacity increases when at ∼900 K straight stripes turn curly toward complex vortex-antivortex domain patterns in the paraelectric phase. At still higher temperatures a low-frequency Drude contribution is triggered by electron hopping signaling an insulator-metal phase transition at ∼1600 K while the MIR response suggests coexistence between single small polarons and bipolarons. On closing, we draw a parallel with improper ferroelectrics sustaining a lattice incommensurate intermediate phase and unit-cell tripling. We argue that in the *h*-$RMnO_3$ (R = rare earth, Y) family of compounds the intermediate phase be considered incommensurate with onset at $T_{INC} \sim 1500$ K and ferroelectric lock-in at $T_C \sim 830$ K delimiting this regime in *h*-$ErMnO_3$.

DOI: 10.1103/PhysRevB.102.134305

I. INTRODUCTION

Multiferroics are a family of materials in which degrees of magnetic and electronic ordering coexist in a common temperature range leading in an ordered phase to control of one property by the other by magnetoelectric correlations [1,2]. Their lattices, in which spin, charge, and phonon arrangements interplay supporting multiferroicity and/or magnetoelectricity, are regularly built by a transition metal and a rare earth in oxygen cages [3,4]. They comprise perovskite distorted lattices undergoing changes eventually leading to stable hexagonal phases that are marginally related to the ideal cubic perovskite. From them, $RMnO_3$, where R is a rare earth or Y, is a distinctive family of compounds sharing properties in topologically related orthorhombic and hexagonal phases. The orthorhombic perovskite arrangement (typically described by the space group *Pbnm*) is no longer stable for rare-earth cations smaller than Tb^{3+} since a hexagonal nonperovskite phase with the same stoichiometry strongly competes in stability [5], being the ferroelectric structure determined by electrostatics and covalency interactions [6,7].

Hexagonal manganites have their 3+ transition metal located at the center of a MnO_5 bipyramid, trigonal bipyramid coordination identified as hexahedra biprims, having fivefold oxygen coordination with no Mn^{3+} Jahn-Teller distortion [8].

*neemmassa@gmail.com

Among these manganites, $ErMnO_3$ is at the borderline between an orthorhombic O-$ErMnO_3$ distorted perovskite and the lattice structure where decrease of the ionic radius, at the *A* site, turns the orthorhombic phase metastable making more competitive a nonperovskite *h*-$ErMnO_3$ hexagonal phase. This yields a noncentrosymmetric lattice belonging to the space group $P6_3cm(C^3{}_{6v})Z = 6$) [5,9] allowing off-center displacements concomitant with ferroelectricity along the *c* axis [4], and a relative high Curie temperature $T_C \sim$ 830 K [10]. Between this temperature and ∼1500 K, above which becomes paraelectric, there is an intermediate phase with residual polarization in which on cooling the bipyramid weakly coupled planes gradually become corrugated by bipyramid tilting leading to low-temperature unit-cell tripling.

The planes house intraplane frustrated magnetic sixfold axis triangular arrangements with Mn moments at ∼120° [11,12]. The antiferromagnetic order sets below T_N at ∼79 K in the Γ_4 representation [13,14]. They are coupled antiferromagnetically along the *c* axis by Mn-O-O-Mn interplay exchange [15].

Although studies of the lower temperature ferroelectric phase have been reported for *h*-$ErMnO_3$ phonons [16,17] and THz magnetic optical activity [18,19], there is no study offering a complete view in the full range of existence yielding a global and better understanding of the electrodynamics of this compound. Here, we report the evolution from low temperatures increasing up to sample decomposition, of main magnetoelectric, lattice, small polaron, and bipolaron features from 5 to 13000 cm^{-1}, i.e., in the sub-THz to mid/near-infrared (MIR to NIR) spectral region using absorption, reflection, and emission spectroscopic methods.

We found in *h*-$ErMnO_3$ strong magnetic field dependencies assigned to M^{3+} moments from 2 to 15 K, in addition to the Er^{3+} manifold peaking [18], earlier identified as dielectric anomalies due magnetoelectric couplings [20], in the same spectral region of a far-infrared reflectivity tail amounting coexistence of hybrid excitations.

From 12 to 300 K, phonon profiles follow the expected for nominal softening and thermal broadening as evidence of strong coupling and anharmonicities. A vibrational mode, with reststrahlen at ∼300 cm^{-1}, undergoes anomalous screening by delocalized carriers that may be assimilated due to Mott electron correlations playing on cooling a polar role, beyond the ion displacements of the noncentrosymmetric $P6_3cm(C^3{}_{6v})$ ferroelectric phase, as the system goes from a Mott-like insulator to an ioniclike insulator in a *de facto* electronic phase transition at T_C [21].

Mode screening suggests strong electron-phonon interactions known for electrons coupling to longitudinal polar modes. We verified this hypothesis using Raman techniques exciting above the gap the $\lambda_{exc} = 355$-nm line. At 300 K a redshifted Fröhlich resonance [22], a sharp band peaking at 322 cm^{-1}, appears at mid-frequency on the infrared macroscopic field plateau associated to the LO $\sim$ 330-cm^{-1} mode.

Our temperature-dependent mid-infrared (MIR) transmission, reflectivity, and emission also corroborate that strong carrier-LO interaction modes yield in *h*-$ErMnO_3$ the fingerprint of quasiparticles named polarons [23,24], and, more specifically, bipolarons [25].

Above $T_{INC} \sim$ 1500 K, the sample gains in opacity as stripes turn into the more complex patterns of the paraelectric centrosymmetric $P63/mmc\text{-}D_{6h}{}^4(Z = 2)$ hexagonal lattice [26]. Increasing the temperature even further, we find the onset of a weak Drude tail marking a metal-insulator transition at $T_{MI} \sim$ 1600 K due to hopping electrons in what may be interpreted as early stages of compound decomposition.

We conclude drawing similarities between *h*-$ErMnO_3$ and the family of improper ferroelectrics, K_2SeO_4 and $X_2ZnCl_4(X = K, Rb)$, that have a lattice incommensurate intermediate phase [27], and suggesting that the delimiting temperatures naming phase transitions at ∼1500 and ∼830 K should be identified as T_{INC} and T_C, respectively, determining the onset of the lattice incommensurate and the "locking-in" in the lower temperature polar phase.

II. EXPERIMENTAL DETAILS

Our *h*-$ErMnO_3$ samples, prepared as polycrystalline powder by a liquid-mix technique, were characterized by x rays and high-resolution Neutron Diffraction Pattern (NDP) which assesses their quality as well crystallized samples with perfectly modeling crystal structures [28]. NDP data were collected at ILL-Grenoble, in the high-flux D20 diffractometer with a wavelength $\lambda = 1.313$ Å. As shown in Fig. 1(a), at ambient temperature each Mn atom is coordinated by five oxygen atoms in a bipyramidal configuration. One O3 atom and two O4 atoms are in the equatorial plane of the bipyramid, whereas the O1 and O2 atoms are at the apexes. Er occupies two crystallographic positions, each bonded to seven oxygen atoms along the *c* axis. The structure for *h*-$ErMnO_3$ consists of layers of corner-sharing MnO_5 bipyramids separated by layers of edge-sharing ErO_7 polyhedra [29]. Figure 1(c) displays the quality of the fit from NPD data, and the inset contains a view along the *c* axis of one layer of MnO_5 units sharing corners forming a characteristic triangular arrangement.

Low-temperature–low-frequency absorbance measurements from 3 to 50 cm^{-1} with 0.5 cm^{-1} resolution have been performed at the THz beamline of the BESSY II storage ring at the Helmholtz-Zentrum Berlin (HZB) in the low-alpha multibunch hybrid mode. Measurements in the 30–300 cm^{-1} range were also taken at the beamline using the internal source of a Bruker IFS125 HR spectrometer. In every case a superconducting magnet (Oxford Spectromag 4000, 10 T (here up to 7 T) interfaced with the interferometer was used for the measurements under magnetic fields [30].

Our preliminary Raman data were taken at 1 cm^{-1} resolution with a Qontor l spectrometer equipped with an Leica 100x microscope objective (NA 0.85) with a 1800 g/mm grating with the 457-nm (Coherent Sapphire single frequency) and 545-nm (Cobolt Fandango^{TM}) exciting lines. The same setup was used with $\lambda_{exc} = 355$ nm but replacing the 1800-g/mm by the 3600-g/mm grating and a Thorlabs LMU-40X-NUV (NA 0.5) focusing objective. The triple subtractive configuration (1800-g/mm gratings) of the Horiba Jobin Yvon T64000 spectrometer allowed Raman acquisition in the low-frequency range up to ∼100 cm^{-1}. In every case laser power on the sample was always less than 1 mW [31].

Near normal infrared spectra were taken on heating using two experimental facilities: one corresponds to reflection and

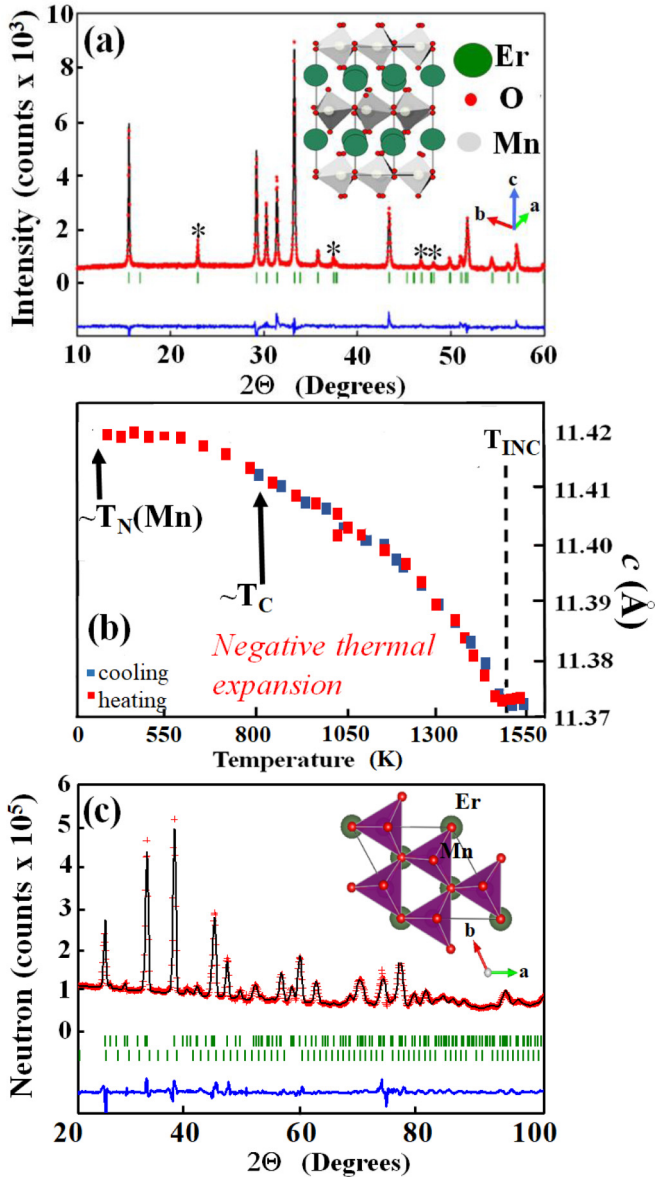

FIG. 1. (a) X-ray (Cu-$K\alpha$) diffraction pattern for room-temperature ferroelectric *h*-ErMnO$_3$ in the space group $P6_3cm(C^3_{6v})$, $Z = 6$. Sharp peaks indicate very good polycrystalline quality without secondary phases. In the Rietveld plot, the red points correspond to the experimental profile and the solid line is the calculated profile, with the differences shown in the bottom blue line. * signals the diffraction peaks of the trimer superstructure. The lattice structure corresponds to a view of the six-formula unit hexagonal lattice [$a = 6.1372(6)$ Å and $c = 11.4209(17)$ Å] with MnO_5 bipyramids plane triangular corner sharing at the nonequivalent O3 and O4 oxygen sites [9]. (b) Negative thermal expansion along the c axis after Ref. [50]. T_C stands for the ferroelectric Curie lock-in temperature and T_{INC} signals the onset of a proposed lattice incommensurate transition (see text). (c) Neutron powder-diffraction profiles at ambient temperature after the Rietveld refinement: red crosses are the experimental points; the solid line is the calculated profile with the differences shown in the bottom blue line. The inset shows a view along [001] of the crystal structure, highlighting the corner sharing arrangement of MnO_5 units in the a-b plane.

a second one to emission. From 12 K to room temperature and from 300 K up to about ~850 K we have measured reflectivity at 1 cm^{-1} resolution with two Fourier transform infrared spectrometers, a Bruker 66 V/s, and a Bruker 113 V, respectively, with conventional near normal incidence geometries. Low-temperature runs were made with the sample mounted in the cold finger of a Displex closed-cycle He refrigerator. For high-temperature reflectivity a heating plate adapted to the near normal reflectivity attachment was used in the Bruker 113-V vacuum chamber. For the low-temperature set an evaporated *in situ* gold film was used as 100% reference reflectivity while a plain gold mirror was used for reflectivity between 300 and 800 K.

Infrared emissivity in the ~500- to ~1700-K range at 2 cm^{-1} resolution was measured with two Fourier transform infrared spectrometers, Bruker Vertex 80v and Bruker Vertex 70, coupled to a rotating table placed inside a dry air box allowing to simultaneously measure the spectral emittance in two dissimilar spectral ranges from 40 to 13 000 cm^{-1}. The sample, which was heated with a 500-W pulse Coherent CO_2 laser, was positioned on the rotating table at the focal point of both spectrometers in a position equivalent to that of the internal radiation sources inside the spectrometers. In this measuring configuration, the sample, placed outside the spectrometer, is the infrared radiation source, and conversely, the sample chamber inside the spectrometers is empty [32–34].

A detailed extended account on the experimental facilities used in collecting data and their analyses for the research reported here may be found in the Supplemental Material [28].

III. METHODS AND DATA ANALYSIS

We retrieve the normal spectral emissivity,

$$\boldsymbol{E}(\omega, T) = \frac{\mathrm{FT}(I_S - I_{RT})}{\mathrm{FT}(I_{BB} - I_{RT})} \times \frac{\mathscr{P}(T_{BB}) - \mathscr{P}(T_{RT})}{\mathscr{P}(T_S) - \mathscr{P}(T_{RT})} \boldsymbol{E}_{BB}, \quad (1)$$

after measuring three I interferograms, i.e., sample I_s; blackbody I_{BB}, and environment I_{RT}, and where FT stands for Fourier transform. $\mathscr{P}$ is the Planck's function taken at different temperatures T, i.e., sample T_S, blackbody T_{BB}, and surroundings T_{RT}. $\boldsymbol{E}_{BB}$ is a correction that corresponds to the normal spectral emissivity of the blackbody reference (a $LaCrO_3$ Pyrox PY 8 commercial oven) and takes into account its nonideality [32].

The temperatures at which the measurements were done were calculated using the Christiansen point, i.e., the frequency where in insulators the refraction index is equal to 1, and the extinction coefficient is negligible. At that frequency, the emissivity E (ω, T), Eq. (1), is set equal to 1, and since the Christiansen point varies its position with temperature, after identifying the frequency for which E $(\omega_{\mathrm{Christ}}, T_{\mathrm{sample}}) = 1$, the only remaining variable left is T_{sample}, the sample temperature that univocally corresponds to it. This procedure becomes a less reliable temperature reference when hopping carriers conceal or distort the frequency minimum.

After acquiring the emissivity data, we placed our spectra in a more familiar near normal reflectivity framework using the second Kirchhoff law, that is,

$$R = 1 - E, \quad (2)$$

where R is the sample reflectivity.

Then, knowing that

$$R(\omega) = \left| \frac{\sqrt{\varepsilon^*}(\omega) - 1}{\sqrt{\varepsilon^*}(\omega) + 1} \right|^2, \tag{3}$$

we calculate the dielectric function from the measured reflectivity or emissivity using a multioscillator fit [35] given by [36]

$$\varepsilon(\omega) = \varepsilon_1(\omega) - i\varepsilon_2(\omega) = \varepsilon_\infty \prod_j \frac{\left(\omega_{jLO}^2 - \omega^2 + i\,\gamma_{jLO}\,\omega\right)}{\left(\omega_{jTO}^2 - \omega^2 + i\,\gamma_{jTO}\,\omega\right)} \tag{4}$$

at every temperature. $\varepsilon_1(\omega)$ is the real and $\varepsilon_2(\omega)$ the imaginary part of the dielectric function [complex permittivity, $\varepsilon^*(\omega)$]; ε_∞ is the high-frequency dielectric constant taking into account electronic contributions; ω_{jTO} and ω_{jLO}, are the transverse and longitudinal optical mode frequencies and γ_{jTO} and γ_{jLO} are their respective damping [37]. The dielectric simulation parameters for h-$ErMnO_3$ showing TO-LO phonons and a broad mid-infrared oscillator band between ~1000 and ~10 000 cm^{-1}, assigned below to polarons, are shown in tables in the Supplemental Material [28]. Note that at higher temperatures, an extra high intensity narrower band corresponding to a *d-d* transition has been added, centered at ~12 000 cm^{-1}, and that for the ~1624-K spectrum we also added a Drude term in the analysis [28].

Next, with the knowledge of individual contributions to $\varepsilon_2(\omega)$, we calculate the real part of the temperature-dependent optical conductivity, $\sigma_1(\omega)$ [38], given by

$$\sigma_1(\omega) = \frac{\omega\varepsilon_2(\omega)}{4\pi}. \tag{5}$$

This constitutes our experimentally measured optical conductivity. Tables I and II show in brackets the phonon reststrahlen mid-value and MIR band ($2^*E_{\text{bipolaron}}$) peak frequencies from the measured reflectivities and emissivities shown in figures and in tables in the Supplemental Material [28]. They then allow a quantitative matching in the MIR to the polaron formalism discussed in Sec. V (Figs. 8 and 9).

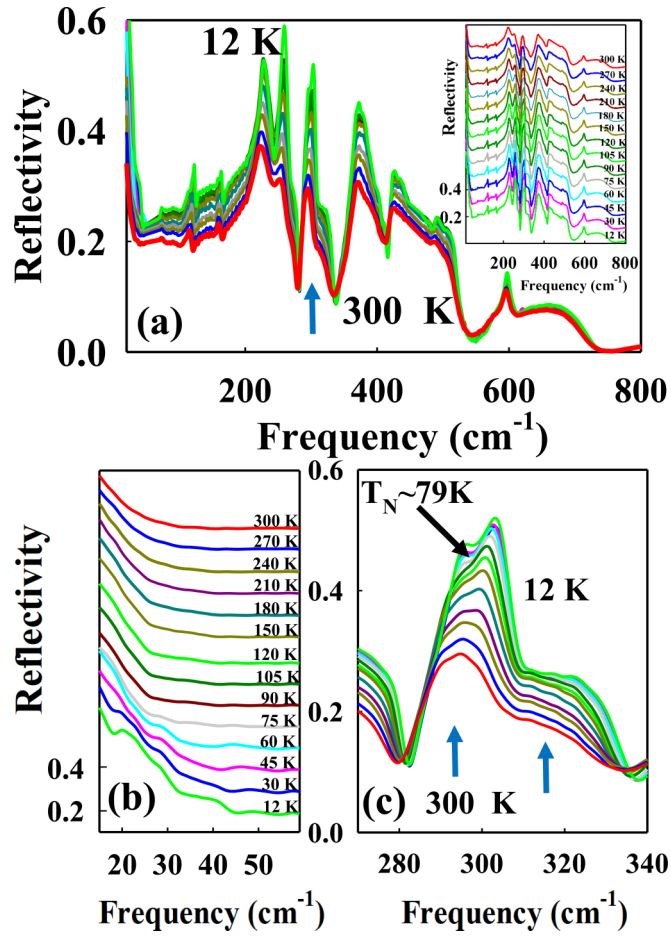

FIG. 2. (a) Phonon near normal reflectivity of h-$ErMnO_3$ between 12 and 300 K (arrow points to the temperature evolution of the anomalous band discussed in the text). Inset: Temperature-dependent far-infrared reflectivity vertically offset; (b) far-infrared band tail assigned to heterogeneity from wall and domain formation (boson peak); (c) band reflectivity showing anomalous plateau steplike shoulder (see text) and phonon split at $T_N \sim 79$ K due to spin-phonon interactions [17] and unit-cell tripling.

IV. RESULTS AND DISCUSSION

A. Low-frequency phonons, magnetic excitations, and Er^{3+} crystal-field transitions in the ferroelectric phase

Figure 2(a) shows the phonon profiles in the lower temperature regime from 12 to 300 K where reflectivity spectra and multioscillator fits (Tables SII–SIV in the Supplemental Material) [28] allow us to identify 21 of the 23 vibrational bands predicted by the irreducible representation for the hexagonal space $P6_3cm(C^3{}_{6v})Z = 6$ [39],

$$\Gamma_{\text{IR}} = 9A_1 + 14E_1. \tag{6}$$

We also corroborate that they undergo an overall regular hardening and band narrowing in close similarity with isomorphous $YMnO_3$ (Refs. [40,41]) and $HoMnO_3$(Ref. [42]). Lattice phonons around 200 cm^{-1} undergo relative intensity changes as the Rare Earth in two inequivalent sites reaccommodate in the ferroelectric phase. Between ~292 and ~340 cm^{-1} there is a set of internal modes from which one has a distinctive reststrahlen screening that will be addressed in the following sections. The strongest of these modes [Fig. 2(c)] gradually splits as the temperature gets close to the antiferromagnetic onset near $T_N \sim 79$ K due to spin-phonon interactions [17] and tripling unit cell. Overall, our spectra, which being from ceramics have A_1 and E_1 phonons superposed, are also in agreement with lower temperature E_1 transverse optical (TO) modes ($E \perp c$) and A_1 listing by Basistyy *et al.* [17].

A more complex environment is suggested by lower frequency near normal reflectivity revealing a well-defined tail of a broad band at THz frequencies [Fig. 2(b)]. We understand the band, THz centered, as arising from structural inhomogeneities, unreleased strains, and potential freer charges localized in grain boundaries or ferroelectric domain walls. The electrical response of the interlocked antiphase boundaries and ferroelectric domains walls is dominated by bound charge oscillations [43]. Vacancies and interstitials may also act as local scattering centers that relate to some structural

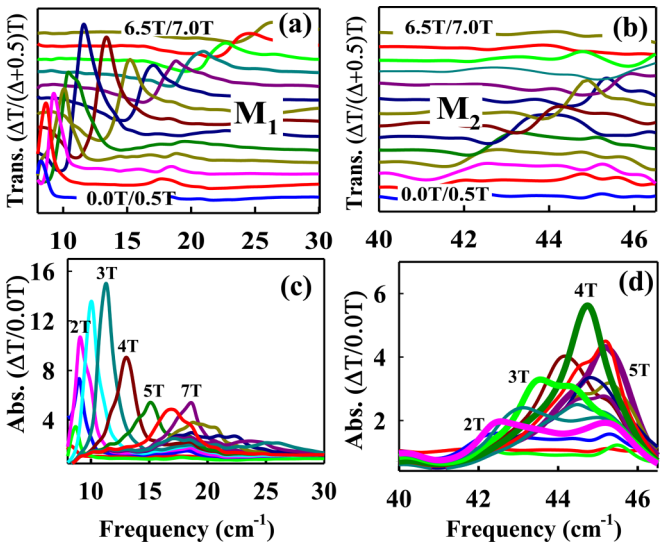

FIG. 3. (a),(b) THz transmission ratio applied field incremental of M_1 and M_2 hardening magnetic excitations in h-$ErMnO_3$ at 5 K [18]. These are out-of-plane Mn moment contributions in a complex $3d$ and $4f$ interplay with Er^{3+} moments at the two nonequivalent Wyckoff sites inferred in the magnetic phase diagram [13,14]. Traces have been vertically offset for better viewing. (c),(d) Same data plotted as absolute ratios relative to the zero-field-cooled signal. Thicker traces in (d) bring up the field-dependent evolution of a net two-site magnetic excitation.

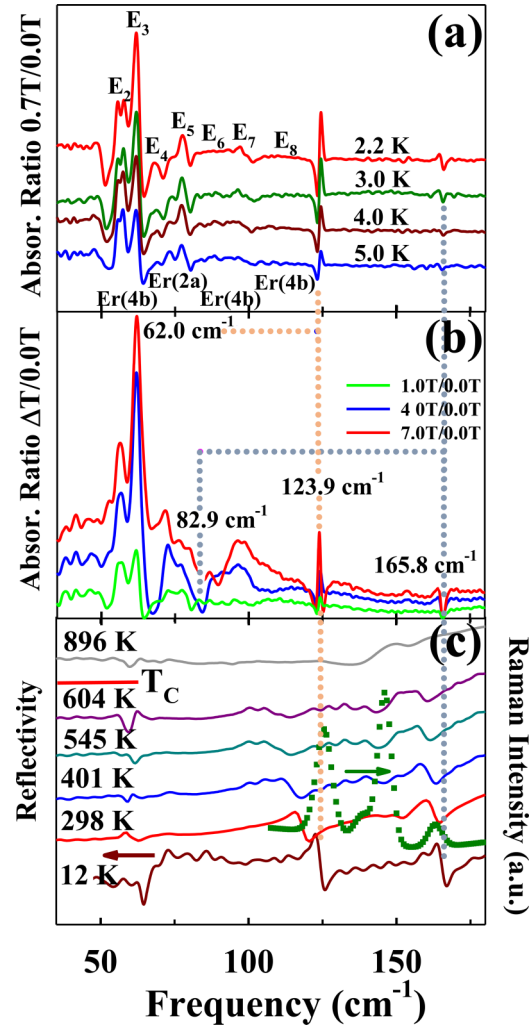

FIG. 4. (a) Far-infrared applied field induced absorption of h-$ErMnO_3$. Crystal-field transitions on the 0.7-T isoline in the ferrimagnetic (2.2, 3.0 K) and antiferromagnetic (4.0, 5.0 K) phases. Traces have been vertically offset for better viewing. Notation after Ref. [18]. (b) 5-K absorption ratio of the strongest Er^{3+} crystal-field transitions at the two sites showing the doubling in energy in dotted lines either in the antiferromagnetic (1 T) or ferromagnetic phase (4, 7 T) [14]. (c) Temperature-dependent weaker bands assigned to magnetic dressed phonons. Full line: Temperature-dependent near normal reflectivity of phononlike features (traces have been vertically offset for better viewing); squares: preliminary Raman-scattering data at 300 K ($\lambda_{exc} = 457$ nm).

disorder at atomic level. Local structural inhomogeneities and an imperfect unit-cell tripling recreate a relaxor-type scenario that may be regarded as a remnant of an incomplete order-disorder phase transition subjected to the ordered polar regions in c axial ferroelectric h-$ErMnO_3$. This heterogeneity is generically known as the origin of the so-called boson peak [44] that is well reproduced in the interval 12 and 300 K by fitting to a Gaussian profile (Tables SII–SIV [28]).

We have also addressed this spectral region in more detail in our BESSY II absorption low alpha runs [28]. Between 2.4 and 5 K the low-temperature magnetic phase diagram of h-$ErMnO_3$ shows field dependent increasing coupling between the Er^{3+} and the out-of-plane Mn^{3+} moments suggesting a complex $3d$ and $4f$ interplay. In this temperature range Er^{3+} moments at the Wyckoff $2a$ site align ferromagnetically along the c axis inducing spin reorientation at Er^{3+} $4b$ and Mn sites. This means going from the Γ_4 into the Γ_2 representation at temperatures lower than T_N [14,45]. Under the umbrella of the Gaussian bell-shaped reflectivity we detect two features, M_1 and M_2, that harden on applied fields that, associated to magnetic excitations, are in agreement with earlier assignments by Chaix *et al.* [18]. Figures 3(a) and 3(b) show the relative effect of applied fields up to 7 T on the M_1 magnonlike excitation as well as the behavior for M_2. In this last case, the band is quite broad with a profile that may be thought as made of several components rather weak and disperse. When increasing fields ferromagnetism is induced [14]; the two-band envelope for 2 T [Fig. 3(d)] suggests spin precessions due to an increment in related anisotropies. Higher fields up to 4 T further increase the magnetic distortion as if reorienting some of them, after which, being overwhelmed by the field, coalesce into one net precessing mode at 5 T with a prevailing spin relative to the spatial direction also found for M_1 mode [Fig. 3(c)]. This suggests a composed scenario by which magnetic moments at rare-earth sites in ferroelectric domain walls create domain-wall magnetism from uncompensated Er^{3+} moments [46] in an environment of fluctuating Mn^{3+} antiferromagnetic order [47].

At slightly higher frequencies, there are crystal-field transitions from Kramers ion Er^{3+} (doublet $4f^{11}$) [48] echoing the two nonequivalent lattice sites. The relative changes induced by the applied magnetic field to the zero-field-cooled spectrum on the 0.7-T isoline are shown in Fig. 4(a). The crystal-field levels of Er^{3+} and several much weaker

features are clearly delineated as the samples pass from being ferrimagnetic to ferromagnetic induced. Our data are in full agreement with Chaix *et al.*, having only a minor energy difference in the E_2 line that resolves when their neutron data are properly deconvoluted [18]. In addition, our spectra point to a remarkable and unexpected correlation between the two most intense of these lines and a couple of higher frequency weaker but sharp peaks. Dotted lines in Fig. 4 show that absorption of the main crystal-field transition of antiferromagnetically coupled Er^{3+}($4b$) at 62.0 cm^{-1}, Fig. 4(b), match a sharper counterpart at exactly the double energy of 123.9 cm^{-1} in either antiferromagnetic (1 T) or ferromagnetic phases (4 T, 7 T) at 5 K. The same kind of correlation, now shown as minima in field depletion, perhaps reflecting the more limited coupling, is observed for Er^{3+} ($2a$) at ∼82.9 cm^{-1} band against 165.8 cm^{-1} respectively. Each pair corresponds to each of the two Er^{3+} ions at the nonequivalent sites. There is also an undefined background continuum that goes unmatched but may be related to interfaces with magnetic and/or electric order parameters moving at unison with the applied field when ferromagnetism is induced in the sample [14].

We also find that those replicas have a remarkable match in our Raman and reflectivity spectra [see Fig. 4(c)] at the same frequencies where two weak and narrow but well defined phonon bands may be traced up to lock-in T_C ∼ 830 K, merging into the high-temperature background. They also agree with phonon profiles in isomorph $YMnO_3$ with Y^{3+} nonmagnetic [40]. That is, by calculating applied to zero-field ratios and comparing with reflectivity and Raman spectra [31] we put in evidence a pure magnetic and phonon electric dipole counterpart of a unique multiferroic excitation. While their specific origin still remains a puzzle (being detected with three independent setups and techniques rules out the possibility of an interferometer or detector artifact) we may reason that these are due to the strong anisotropies between the rare earth and oxygens involved in plane buckling and bipyramid tilting in conjunction with the dynamics emerging from the c-axis negative thermal expansion [49] and, perhaps, also associated to reinforcing ferroelectricity, the $4f^{11}$-$3d^4$ interplay being a known player in polar ordering [45] in an ongoing process with imperfect $(\sqrt{3} \times \sqrt{3})R30^\circ$ structural ordering [50]. It points to symmetry allowed lattice phonon interactions with $4f$ electrons associated to ground Er^{3+} crystal-field levels that is better seen at low temperatures due to the increase in their population. Very recently, Singh *et al.* [51] reported that in double perovskite Nd_2ZnIrO_6 low-lying excitations amount to strong coupling between phonons and $Nd^{3+}4f^3$ crystal-field excitations raising the possibility that all these magnetic and lattice degrees of freedom have common ground that might also be shared by features found in $HoMnO_3$ [52].

B. Screening of an optical-phonon reststrahlen

Oxides have a strong tendency toward delocalized p oxygen states in which the interplay of Coulomb and electron-phonon interaction leads to a ferroelectric instability [53]. It is known that the origin of the anisotropies in the ion polarizability lies in the O^2 instability as a free ion [54,55]. It means that in the h-$ErMnO_3$ lattice forming a closed $2p$ 6 shell oxygen needs neighboring Mn and rare earth. Within this context, as it is shown in Fig. 6, most lattice and bipyramid internal modes continue above room temperature the softening and thermal broadening trend already shown between 12 and 300 K [Fig. 2(a)]. The distinctive exception is a narrower and strong asymmetric profile that between 292 and 333 cm^{-1} (Table SII [28]) has a lower intensity steplike plateau on the higher frequency side. This is the vibrational region with A_1 and E_1 internal modes mainly involving in- and out-of-plane oxygen motions [16,39,41,42] that through hybridization add to the net polar distortion. The shoulder remains partially screened approaching room temperature in a split mode picture [Fig. 2(c)] while it decreases approaching ∼830 K to become almost fully screened at ferroelectric lock-in T_C (arrow in Fig. 5). The result is an asymmetric profile that may still be fitted with a single oscillator (Table SVII [28]). In the intermediate phase, between ∼830 and ∼1500 K, Figs. 5 and 6(a), it becomes barely distinctive from a horizontal trace pointing to a strong anomaly in the reststrahlen macroscopic field associated zone center ∼273 cm^{-1} longitudinal-optical mode (1119 K, Table SVIII [28]).

We recall that a reststrahlen macroscopic field arises from the long-range Coulomb interaction responsible for the transverse optical-longitudinal optical (TO-LO) split. It may be though as if the LO mode were backed by long-range electric fields appearing as an extra restoring force due to a Coulomb interaction. The net result is the increase of the longitudinal-optical mode frequency. It implies a relative displacement of charged ions in the lattice unit cell generating a macroscopic field that can then be expected to interact with electrons. The interaction between an electron charge and the macroscopic Coulomb potential is known as Fröhlich interaction [56].

It is also known that carrier mobility in a polar lattice is reduced by coupling to LO modes via Fröhlich interaction in what may be basically understood as due to a polar lattice-charge-carrier electrostatic interaction leading by localization to the formation of small polarons. Thus, when the macroscopic field gets electron screened the TO-LO split becomes narrower, reducing the phonon oscillator strength as observed. Figure 6(a) and supplemental Figs. S11 and S12 [28] show that close to the paraelectric phase transition, up to ∼1500 K, there is already no trace of this phonon. At these temperatures the main change corresponds to lattice modes around ∼190 cm^{-1} gradually merging into one symmetric broad band denoting a sole rare-earth crystallographic position onset of the paraelectric phase with a net inversion center not allowing off-center displacements.

C. Fröhlich Raman resonance

As h-$ErMnO_3$ at room temperature is a noncentrosymmetric polar compound, the infrared active modes are also Raman zone-center allowed implying that we may further pursue the characterization of the anomalous reststrahlen screening by measuring its Raman activity. It is known from earlier studies on hexagonal semiconductors that charge density fluctuations of free electrons couple to the macroscopic longitudinal electric field of infrared active polar optical lattice vibrations and that the resulting coupled modes have a mixed plasmon-phonon character [22]. Phonon-plasmon coupling was intensely studied, optimizing the cross section by

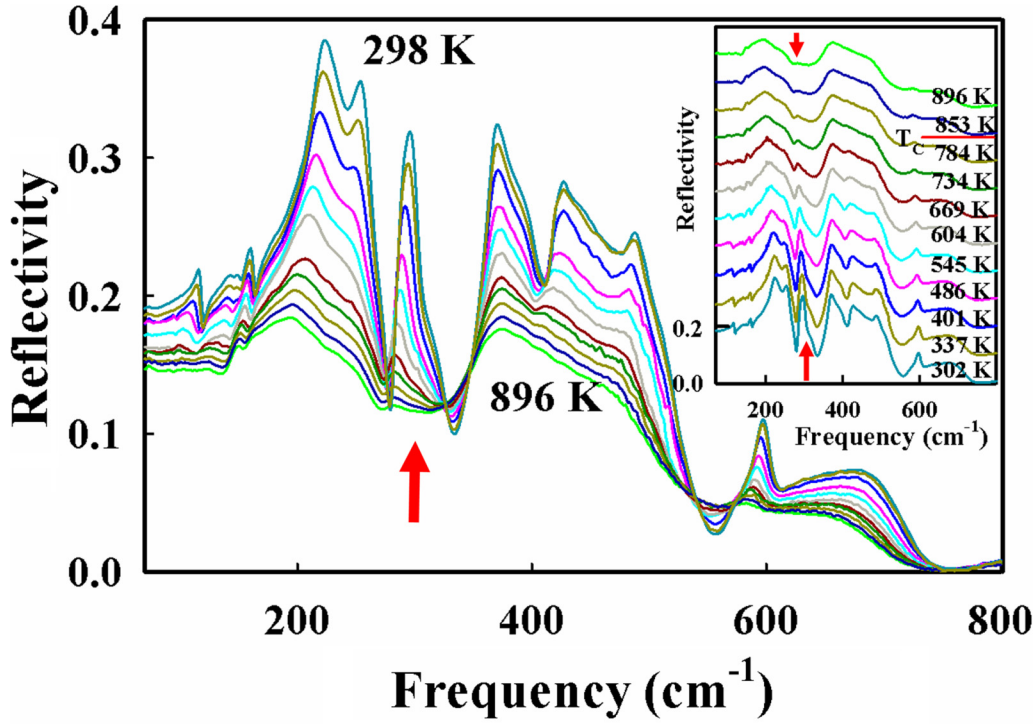

FIG. 5. Reflectivity of h-$ErMnO_3$ between 298 and 896 K (arrow points to the temperature evolution of the anomalous band profile). Inset: Overall temperature-dependent far-infrared reflectivity vertically offset with arrows pointing to the softening of the anomalous band.

choosing exciting laser lines with energies above the semiconducting gap, in which case, the zone-center LO mode cross section is strongly enhanced via Fröhlich interaction, again, the interaction between an electron charge and the macroscopic Coulomb potential [22].

First-order Raman-active zone-center modes of h-$ErMnO_3$ belong to the irreducible representation [39],

$$\Gamma_{\text{Raman}} = 9A_1 + 14E_1 + 15E_2. \tag{9}$$

These Raman phonon profiles are heavily dependent on the excitation line and have as a dominant feature the bipyramid breathing and its overtone. This A_1 683-cm^{-1} mode ($\lambda_{\text{exc}} =$ 457 nm, 300 K), Fig. 7(a), involves c-axis apical O1-O2 ion displacements creating an effective polar distortion in the MnO_5 bipyramids along interplanar ferroelectric c direction [42]. It is associated to the transition between $xy(x^2 - y^2)$ and $3z^2 - r^2$ orbitals by which the occupation of the $3z^2 - r^2$ orbital creates a Coulomb repulsion enhancing the breathing relative to the Mn^{3+} ions in the plane [16]. Our room-temperature spectra [Fig. 7(a)] are in overall agreement with earlier Raman data [31].

Here we will limit our comments to the spectral range specific to the region in which we observed the unusual changes in the infrared spectra commented on in the preceding paragraphs [31]. Specifically, we use a 355-nm laser exciting line aiming to avoid the interference of electronic transitions in the cross sections. It allows the detection of a strong unambiguous quasiresonant band [Fig. 7(b)] emerging near the middle frequency of the reststrahlen band down from the LO frequency that may be straightforwardly associated to the carrier screening. TO modes in the ferroelectric phase are both Raman and infrared active while the LOs are Raman active only. The peaking at 322 cm^{-1} is at shoulder mid-frequency of the infrared reflectivity where the mode at 297 cm^{-1} (TO) may be used as a reference to confirm the agreement between Raman and infrared spectra [Fig. 7(b), inset]. The LO resonance is redshifted relative to the infrared minimum because of the presence of carrier screening of the macroscopic field, Landau damping, in the polar environment suggesting the association with conclusions by Abstreiter *et al.* on n-type, p-type Si, Ge, and n-type GaAs semiconductors [22,57–59]. It is however worthwhile to note that our band screening is due to delocalized carriers subjected to the dynamics of the negative thermal expansion in an environment prone to strong polaron coupling and weaker deformation potential mechanisms involving intraband excitations of carriers as shown in the following sections.

D. Negative c-axis thermal expansion

A dynamical perturbative mechanism that requires attention in our analysis is in the uniaxial negative thermal expansion reported in the h-$RMnO_3$ (R = rare earth, Y) family of compounds [50,60–64].

The relative negative lattice distortion along the c axis, Fig. 1(b), is stronger in the intermediate phase, where the structural trimerization involves Mn and O ion displacements through plane buckling due to mismatched Er ions. At about the lock-in temperature it turns gradually into a more lower temperature moderate regime [50,60].

Negative thermal expansion is understood as due to rigid polyhedral lattice units performing a quasirigid rotation (libration) [65,66]. These polyhedra in h-$ErMnO_3$ are MnO_5 bipyramids in which the corner sharing bridging oxygen in

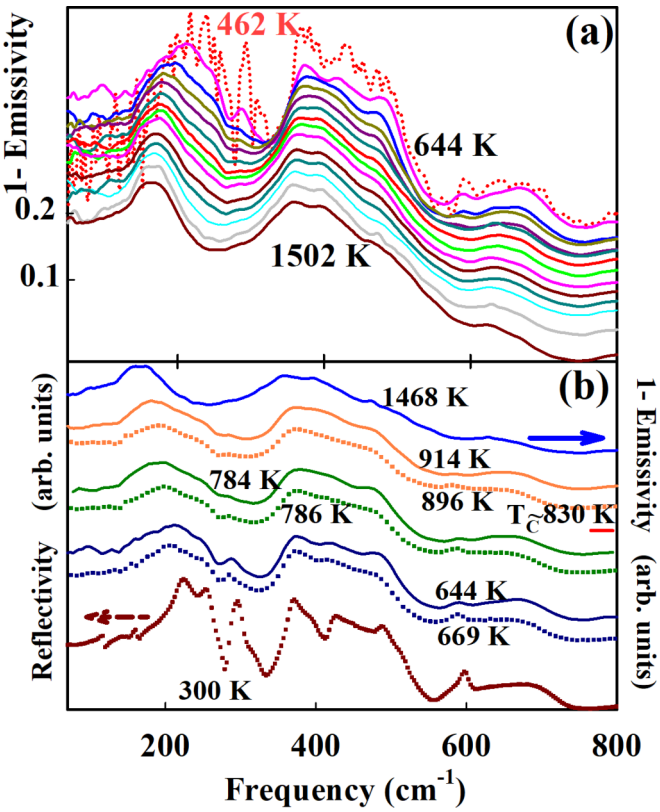

FIG. 6. (a) Near normal 1-emissivity of h-$ErMnO_3$ between 462 and 1502 K. Note that although at 462 K (dotted line) the sample is not hot enough to yield a less 1-emissivity noisy spectrum it is in full agreement with phonons in Fig. 5. The spectra have been vertically offset for better viewing. (b) Overall phonon behavior from ambient to 1468 K overlapping near normal reflectivity and 1-emissivity absolute values in the common temperature range. Squares: reflectivity; full lines: 1-emissivity.

M-O-*M* links may be seen pivoting as a hinge dynamically increasing the oxygen amplitude. This, by purely geometric arguments, reduces the x-ray measured bond length of the true lattice constant, since now it appears as a shorter distance when the bond is subjected to positive and negative strong fluctuations [67,68]. For h-$ErMnO_3$ we associate this motion to vibrational modes centered around 290–370 cm^{-1} involving upward motions of the O ions (and Mn) in the stiffer bipyramid sublattice [16,62]. Band broadening and softening anharmonicity in other phonons mostly contribute to positive thermal expansion but sharper band changes around the ~370 cm^{-1} internal mode region, near and below T_C, also indicate processes for which the bipyramids may be better thought of as quasirigid units. The out-of-plane displacements add to ferroelectricity [26] considering oxygen ions polarizable objects [53–55].

In a more quantitative picture, the gradual evolution of the screening in the ~322 cm^{-1} TO-LO macroscopic field split would be then an indication of a disruption in the strong electron-electron correlations in h-$ErMnO_3$. Local reststrahlen screening would be tied to the sublattice motion singular to negative thermal expansion. Below ~830 K the negative thermal expansion along c gradually allows electrons to add coherently to the polar mechanism of the already present noncentrosymmetric rare-earth displacements that is at the structural origin of ferroelectricity below ~1500 K.

This scenario connects our compound to earlier ideas on the possibility of a Mott semiconductor [69] having a ferroelectric instability [70] and assimilates this to dynamically disrupted local electron-electron interactions of Mott charge carriers inducing Coulomb screening in the reststrahlen TO-LO split. Those carriers gradually coalesce condensing into collective charge localization and ordering locking in ferroelectric electrons below $T_C \sim 830$ K. Basically, this may be then understood as a locking-in electronic process for a macroscopic spontaneous polarization response of highly correlated electrons [21]. However, our spectra show that band sharpening of the internal modes is not limited to the screened mode but rather extends to the neighboring vibrational modes that emerge as sharper bands (Fig. 5) below T_C from the contour that it is already outlined in the intermediate higher temperature phase (Figs. 5 and 6). This is a known activity for phonons in ferroelectric insulators sustaining an incommensurate phase and tripling of the unit cell [71]. For this reason, and although this behavior compounds with the dynamics imposed by the negative thermal expansion, we propose that $T_C \sim 830$ K in h-$ErMnO_3$ be considered as a lock-in Curie temperature.

Ferroelectric coherent order is reduced on heating above $T_C \sim 830$ K at the change in the slope of the uniaxial negative thermal expansion in what amounts to a c dynamic contraction of oxygen-erbium bonds at a temperature range in which, as described in the next section, there is a change on cooling from a bipolaron to a more localized small polaron regime. It is also appealing to think that the anomalies observed may relate to local bond conductivity increments in an environment for which low disorder increments break down an initial Mott insulating system as recently predicted for interacting systems [72].

E. Small polaron and higher temperature bipolarons

We have seen in previous sections the main role of electron-lattice correlations that may also be functional to the magnetic order. This merits the extension of our quantitative look to the mid-infrared region (MIR) where electron-phonon interactions in the ferroelectric environment are key for revealing quasiparticles named small polarons [73].

A small polaron is made of an electron laying in the ion potential created by the disturbance that the charge carrier creates. Short-range electron-phonon interactions are paramount [74].

Its optical detection is due to a self-trapped carrier excited from its localized state to a localized state at a site adjacent to the small polaron site. The small polaron range is usually less than the unit-cell size having as a main transport property a characteristic thermal activated hopping accompanied by the lattice deformation. The implied picture is found in systems than range from oxides to polymers and has been the subject of many reviews [24,25,75].

As already pointed out in the Supplemental Material Methods and Data Analysis section [28], our reflectivity (or 1- emissivity for measured emission) multioscillator fits

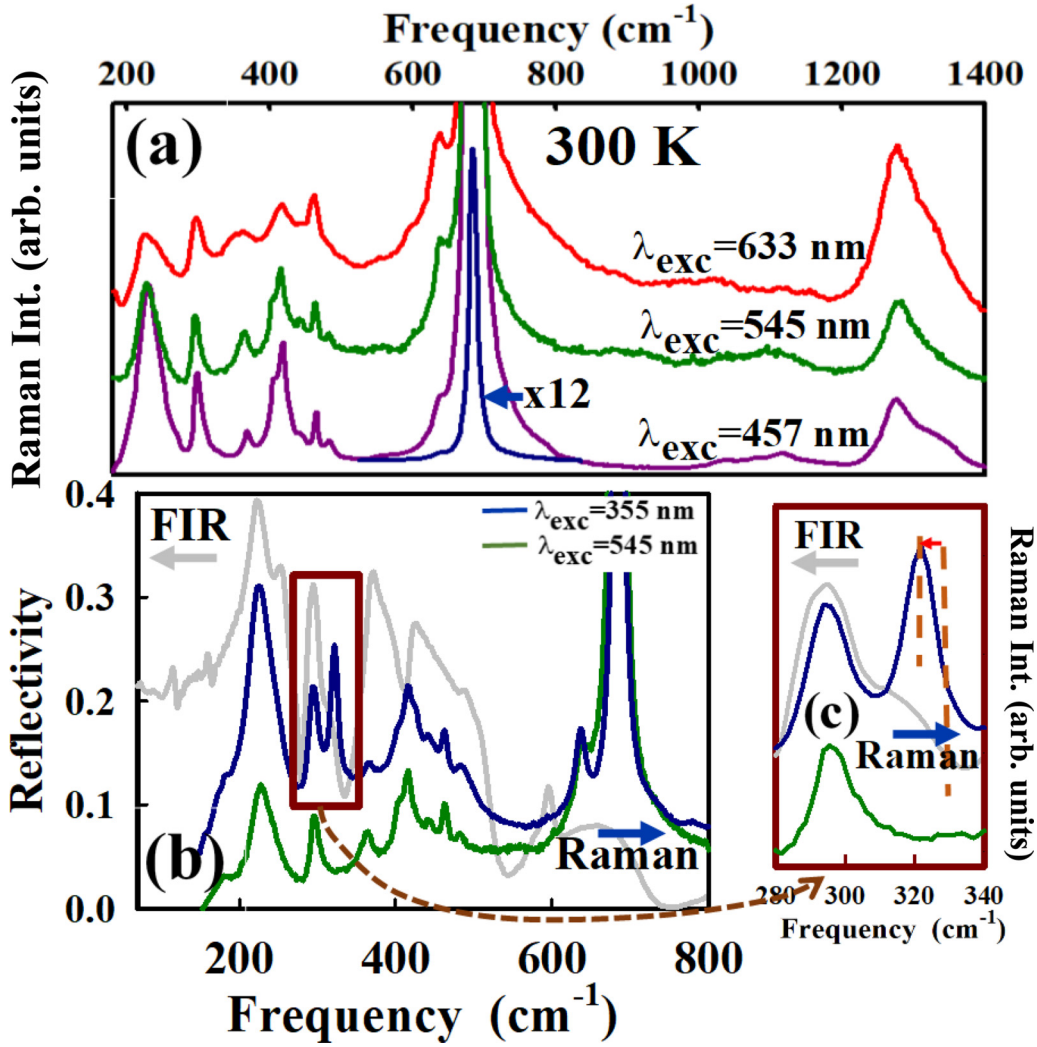

FIG. 7. (a) h-ErMnO$_3$ Raman spectra cross section dependence using exciting laser lines $\lambda_{exc} = 457$, 514, and 633 nm at 300 K. (b) Comparison of Raman spectra obtained using $\lambda_{exc} = 355$ nm and $\lambda_{exc} = 514$ nm laser lines. The same sample far-infrared reflectivity is outlined in the background in lighter gray trace. Inset (c) at the right Detail showing charge carriers causing redshift (dashed vertical lines) of the Raman active LO mode using $\lambda_{exc} = 355$ nm assigned to a Fröhlich resonance. FIR reflectivity counterpart is outlined in lighter gray trace.

yield individual contributions to the imaginary part of the dielectric function, $\varepsilon_2(\omega)$, that in turn, allows using Eq. (5) to calculate the real part of the temperature-dependent optical conductivity, $\sigma_1(\omega)$, spanning from the far- to the mid-infrared. As it was stated, this constitutes our data from which the mid-infrared will be examined in terms of polaron quasiparticles.

Our starting point for matching the experimental optical conductivity is the known formulation by Reik and Heese for small polarons [23,76]. Here, small polarons are addressed microscopically as due to nondiagonal phonon transitions. The optical conductivity is calculated for carriers in one small band and interband transitions are excluded. Starting with a Holstein´s Hamiltonian [77], the frequency-dependent conductivity is calculated using Kubo´s formula [78,79]. The real part of the model optical conductivity for a finite temperature T, $\sigma_1(\omega, \beta)$ is given by

$$\sigma_1(\omega, \beta) = \sigma_{DC} \frac{\sinh\left(\frac{1}{2}\hbar\omega\beta\right) \exp[-\omega^2\tau^2 r(\omega)]}{\frac{1}{2}\hbar\omega\beta[1 + (\omega\tau\Delta)^2]^{1/4}}, \tag{10}$$

$$r(\omega) = \left(\frac{2}{\omega\tau\Delta}\right) \ln\{\omega\tau\Delta + [1 + (\omega\tau\Delta)^2]^{1/2}\} - \left[\frac{2}{(\omega\tau\Delta)^2}\right]\{[1 + (\omega\tau\Delta)^2]^{1/2} - 1\}, \tag{11}$$

with

$$\Delta = 2\varpi\tau \tag{12}$$

and the relaxation time

$$\tau^2 = \frac{\left[\sinh\left(\frac{1}{2}\hbar\varpi\beta\right)\right]}{2\varpi^2\eta}. \tag{13}$$

That is, our model conductivity, $\sigma_1(\omega, \beta)$, $\beta = 1/kT$, is bell-shaped quasi-Gaussian three parameter dependent; $\sigma_{DC} = \sigma(0, \beta)$, the nominal electrical DC conductivity, the frequency ϖ_j that corresponds to the average between the transverse and the longitudinal optical mode of the jth reststrahlen band, and η is a parameter characterizing the strength of the electron-phonon interaction, i.e., the average number

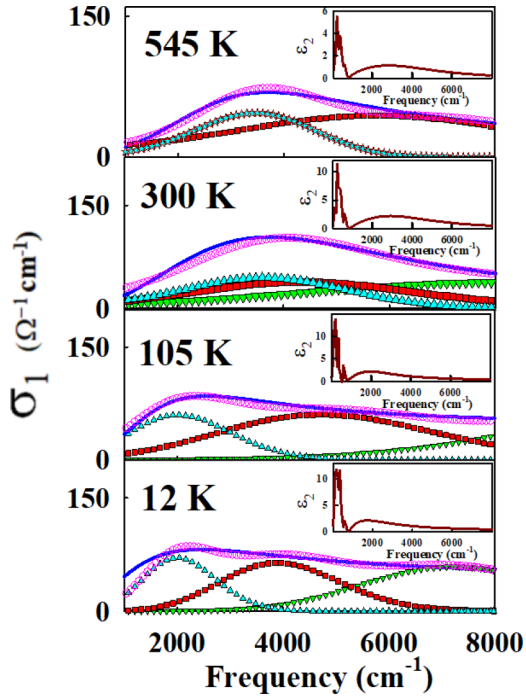

FIG. 8. σ_1 real part optical conductivity at 545, 300, 105, and 12 K in the ferroelectric phase (full line: experimental; open circle: full fit; square, upper, and lower triangles are the individual quasi-Gaussians reproducing the experimental optical conductivities with the parameters shown in Table I; the 545-K open circle envelope is the fit by bipolaron [solid starts, Eq. (14)] and small polaron [Eq. (10), solid square] contributions while only small polaron quasi-Gaussians, Eq. (10), are needed at 300, 105, and 12 K. Insets: Full spectral range of the measured dielectric function imaginary part ε_2.

of virtual phonons contributing to the polarization around a localized polaron. These are in Eq. (10) the adjusting parameters to the MIR for experimental conductivity extracted in the analysis of the reflectivity (or 1-emissivity for measured emission). It allows us to identify the phonon frequency ϖ_j associated to the polaron from those out of the listing modes shown in fit tables in the Supplemental Material [28]. η_j, which constitutes the only true free parameter, is also proportional to the small polaron binding energy $E_b = \eta\varpi_j/2$. The other constant, $\sigma_{DC} = \sigma(0, \beta)$, is just a multiplier factor [80]. $\eta \sim 3$ implies a weak electron-phonon interaction while a value around 14 or higher would correspond to the very strong end [81].

To reproduce the full mid-infrared spectral region, we then allowed the possibility of more than one vibrational contribution using an empirical approach, shown successful when applied to other distorted perovskites and glassy systems [82–84]. This results in the convoluted addition of bell shaped uncorrelated individual contributions in the region from 1000 to 9000 cm^{-1}, each calculated at a phonon frequency ϖ_j associated to the strength η_j at a temperature T.

A good fit of the experimental optical conductivity of h-ErMnO$_3$ at 300 K requires a full small polaron approach with torsional (319 cm^{-1}), breathing (735 cm^{-1}), and overtone (1480 cm^{-1}) as distinctive vibrational frequencies (Fig. 8, Table I) for each quasi-Gaussian. Discussed in previous sections, these peak positions correspond to the band with the anomalous reststrahlen and the interplane ferroelectric mode (and its overtone) respectively. The same picture holds down to about 100 K where reflectivity [Fig. 2(c)] shows that the unscreened portion of the band profile from 290 to 330 cm^{-1} starts splitting due to spin-phonon interactions [17] and the ongoing unit-cell tripling. At 12 K only invoking independent vibrational group modes satisfies the mid-infrared response shown in Fig. 8 that is also seen in overall sharper defined reflectivity (Fig. 2). All parameters used in the computation of these lower temperature optical conductivities are collected in Table I. Below each frequency ϖj we also added in brackets the mid TO-LO split measured frequency, from the reflectivity fit, shown in tables for 300, 109, and 12 K in the Supplemental Material [28]. In every case, our η_j's, the parameter characterizing electron-phonon interactions, are found in the strong regime concomitant with the Raman measurements discussed in Sec. IV C on the Fröhlich resonance.

On the other hand, increasing temperature yields MIR profiles that cannot be totally satisfied by only the quasi-Gaussian small polaron contributions under consideration. At 545 K, (Fig. 8) still below the ferroelectric lock-in temperature, we

TABLE I. Parameters of small polaron fits to the h-ErMnO$_3$ experimental optical conductivity at 545, 300, 105, and 12 K (see text). Note that resulting vibrational frequencies $\varpi_{phj}(j = 1, 2, 3)$ are in agreement with the experimental reststrahlen mid-value frequencies shown in brackets. The DC conductivity σ_{DC} in Eq. (10) was kept as a fit constant.

T K	σ_{DC} (ohm^{-1}cm^{-1})	η_1	ϖ_{ph1} (cm^{-1})	η_2	ϖ_{ph2} (cm^{-1})	η_3	ϖ_{ph3} (cm^{-1})
~1624	87	7.4	438.3 (438.1)	11	645.0 (644.4)		
545	8			11.2	707.2 (696.8)		
300	7	13.5	318.9 (326.9)	7.6	735.0 (680.5)	7.3	1480
105	7	7.8	330.8 (329.9)	8.55	686.8 (682.1)	13.7	1472.0 (1364.3)
12	40	11.70	198.5 (222.8)	15.0	290.1 (312.9)	19.2	411.0 (421.2)

TABLE II. Parameters used in the bipolaron simulation fits for h-$ErMnO_3$ mid-infrared optical conductivity. σ_{DC} in Eq. (14) was used as fit fixed parameter. Corresponding experimental frequencies appear in brackets below model values.

T (K)	$2^*E_{bipolaron}$ (cm^{-1})	$\sigma_{DC}(\Omega^{-1}\,cm^{-1})$	$\omega_{(vib)}$ (cm^{-1})
545	3799 (3805)	2.5	302 (295.3)
906	2778 (2509)	79	277 (280.3)
1119	3775 (3475)	36	270 (271.4)
1298	3998 (3727)	68	352.3 (354.5)
1578	4784 (4436)	37	415 (420.1)
~1624	2590 (2305)	86	412 (438.1)

found that in addition to a small polaron quasi-Gaussian with the $\sim 707\,cm^{-1}$ breathing vibrational mode (Table I) it was necessary to add a bipolaron term (Table II) for reproducing the lower frequency portion of the optical conductivity, meaning that intermediate-temperature conductivities reflect different degrees of localization and coexistence in a changing stripe/vortex environment [26].

A bipolaron is made of two small polarons in association as a two-carrier self-trapped localized bound pair, in which the common potential exceeds their Coulomb repulsion [84]. In this regime the confinement energy of small bipolarons is double relative to that in small polarons because of the presence of the second electron, i.e., the depth of the well that self-traps both carriers is twice as deep. Their effective mass is expected to be also much larger than the hundredfold increments of the electron mass expected for small polarons [24,74,85,86].

The electron-phonon coupling energies are quadrupled, and at the same time, both charged carriers repel through their U- Coulomb interaction, i.e., the bipolaron is stable if $2E_b > U$. Accordingly, band peaking associated to bipolarons is found at higher frequencies than for small polarons [87]. This means that for small bipolarons the $2E_b$, the peak energy of the small polaron absorption, has to be replaced by $2E_b' = 4E_b - U$, the frequency of the measured absorption (conductivity) maximum, and Δ by $\Delta' = \sqrt{2E_b' E_{vib}}$, where E_{vib} corresponds to a relevant mediating phonon [24]. Using this simplified version for the optical conductivity, that supplies the absence of the microscopic approach but retains the basic concept of Reik's small polaron original proposition, reads

$$\sigma(\omega, T) = \sigma_{DC}\frac{\sinh(4E_b'\hbar\omega/\Delta'^2)}{4E_b'\hbar\omega/\Delta'^2}\exp[-(\hbar\omega)^2/\Delta'^2], \quad (14)$$

where $\sigma_{DC} = \sigma(0, \beta)$, $\beta = 1/kT$ is again the electrical or optical DC conductivity.

We found that this formulation reproduces the MIR optical conductivity between the Christiansen point and the absorption edge of the Mn $d_{x^2-y^2,xy} \rightarrow d_{3z^2-r^2}$ transition in our highest temperature regime of the emission measurements. Our bipolaron band profiles are similar to the ones earlier reported for other oxides [88,89]. However, unlike in distorted perovskites, where a successful fit requires the octahedral breathing frequency $\sim 700\,cm^{-1}$ for the bipolaron mediating phonon $\omega_{(vib)}$, in h-$ErMnO_3$ we need to replace that value for a frequency close to that anomalous band at $\sim 322\,cm^{-1}$. This brings the quasi-Gaussian [Eq. (14)] to agreement with the optical conductivity from measured 1-emissivity. Figure 9 shows these at different temperatures in the intermediate region between ~830 and ~1500 K and in the paraelectric phase at 1545 K. $2E_b'$ from model fit and 1-emissivity (in brackets) are listed for each temperature in Table II. It can be seen that the bipolaronic band hardens between ~700 and ~1200 K. Further up in temperature the opacity in the compound increases flattening the profile, which starting at ~1300 K is seen as prompting a discontinuity toward the paraelectric phase. The MIR evolution reflects the stripe from orderly aligned stripes to the curly, close to T_{INC}, to the articulated vortex-antivortex domain structure pattern reported in the paraelectric phase for h-$ErMnO_3$ [26].

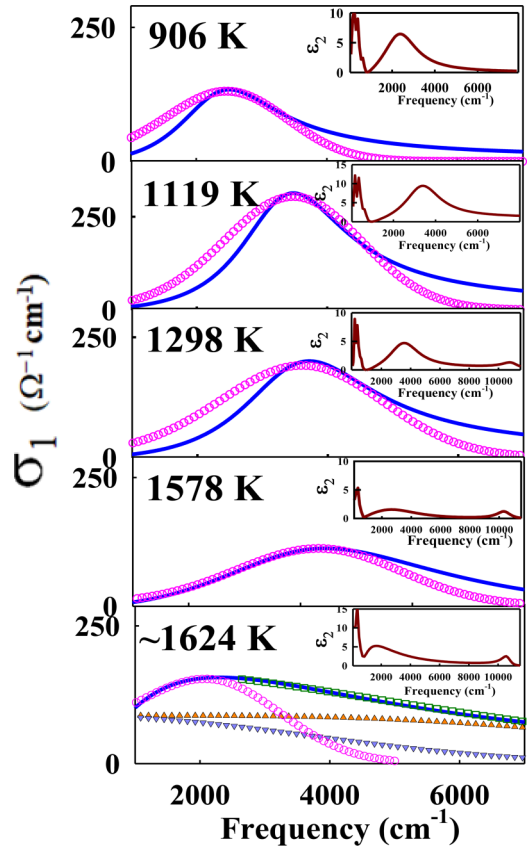

FIG. 9. σ_1 real part optical conductivity at 906, 1119, and 1293 K in the intermediate phase [full line: experimental; open circles: fits by Eq. (14)]. Insets: Full spectral range imaginary part ε_2 of the measured dielectric function. The relative increase in opacity at 1578 K, in the paraelectric phase, is in accordance with the appearance of vortex-antivortex domain structure reported at about these temperatures [26]. The real part of the optical conductivity at ~1624 K is shown in the lowest panel (full line: experimental; circle and open square: fits). The plain superposition of the two formulations, bipolaron [full line: experimental; open circles: fit by Eq. (14)] and small polaron [solid triangles: fit by Eq. (10)] suggests coexistence (see text). Inset: full spectral range imaginary part ε_2 of the measured dielectric function.

At 1578 K (Fig. S9 [28]) our optical conductivity fit (Fig. 9) yields a frequency at ∼415 cm^{-1} to reproduce the experimental data. This frequency matches the average of the three torsional bipyramid internal modes (asterisks in Table SX [28]) that have as a common denominator the oxygen ion displacements, these being part of the five detected out of six zone-center modes, $\Gamma_{IR} = 3A_{2u} + 3E_{1u}$, predicted by group theory for the space group $P6_3/mmc(D^4_{6h})$ in the paraelectric centrosymmetric phase [39].

Increasing the temperature further, Fig. S10 [28] shows that electron hopping induces a lower frequency Drude term [Eq. (S5) [28]] onset of an insulator-metal phase transition at ∼1600 K in a sequence that at still much higher temperatures leads to sample decomposition. This effect, as well as possible embedded temperature induced defects [82], increases conductivity prompting an insulator into an incipient poor conducting solid yielding a quantitative picture for a thermally driven insulator-metal phase transition. The new tail in the far infrared, as pointed out in Sec. II, also reduces the usefulness of the Christiansen point as a functional thermometer [28].

Above 1600 K, Fig 9, the bipolaron peak position softens yielding a mid-infrared spectrum that beyond ∼3000 cm^{-1} is an undistorted tail up to 10 000 cm^{-1} similar to the a mid-infrared response for single small polarons (Fig. 8) suggesting localization in an intermediate regime for a many-body scenario. In this scenario one of the dimerized electron pair constituting the bipolaron hops to a next-nearest-neighbor small polaron site changing the mid-infrared profile within a picture that turns indistinguishable from what we already reported for the high-temperature metal-insulator transition in orthorhombic O-$ErMnO_3$ at about the same temperatures [89]. I.e., as shown in Fig. 9, the reproduction of the optical conductivity at ∼1624 K is a plain superposition of a contributions product of the bipolaron dissociation as for small polarons coexisting with Drude thermal activated itinerant carriers. The small polaron parameters used in this fit are shown in Table I while those for the bipolaron band are in Table II.

V. CONCLUSIONS

In an effort to get a more comprehensive picture on multiferroic $ErMnO_3$ in its hexagonal phase we studied the infrared response using absorption, reflectivity, and emissivity techniques in its full range of existence. An intriguing phonon magnetic convergence was found at the lowest frequency modes. Phonons, whose detection extends up to the onset of the intermediate phase, correspond to well defined magnetic replicas of Er^{3+} crystal-field transitions suggesting strong magnetoelectric couplings.

Our measurements show that in addition to the known ion displacement in MnO_5 bipyramid buckling, and rare-earth vertical shift away from the high-temperature mirror plane [9,26], there is a dynamical bond instability related to ferroelectric order. Its origin is potentiated by the oxygen intrinsic polarizability [54,55,90] bringing up a critical interplay of ionic and electronic interactions to a common ground with that reported for many ferroelectrics [73].

A most distinctive temperature-dependent phonon profile is found associated with a torsional mode involving oxygen displacements dynamically correlated to the negative thermal expansion along the *c* axis [50,60]. It has a nearly fully screened macroscopic field in the intermediate phase where it is also found mediating in bipolaron conception. Below the lock-in ferroelectric transition at ∼830 K it turns into a well-defined asymmetric band, at 288–329 cm^{-1} (300 K), that having one remaining component partially screened further splits as spin-phonon interactions become significant and the unit-cell tripling takes place. Its existence implies an environment revealing a delicate balance of long- and short-range interactions that compounds with local disruptions of the strong Coulomb electron repulsion in the noncentrosymmetric entangled phase. Concomitant with this, but using Raman scattering excited with λ_{exc} 355 nm above the gap laser line, we verified strong electron-phonon interactions via a Fröhlich resonance at 322 cm^{-1} induced by carrier delocalization interplay with the Coulomb originated TO-LO split of the corresponding screened reststrahlen. This phonon also remains a fundamental feature when the high-temperature bipolaron regime turns to small polaron. At these temperatures, the MIR optical conductivity is reproduced using Reik's formulation [23]. Accordingly, we associate that vibration with a primary order parameter.

At 1578 K, in the paraelectric phase, we found that a fit using a vibrational frequency at ∼415 cm^{-1} results in an almost perfect matching with the experimental optical conductivity. This frequency corresponds to the average of three main torsional bipyramid internal modes (Table SX [28]) involving oxygen displacements. High-temperature MIR profiles change as the sample opacity increases when straight stripes turn curly toward more complex domain figures above ∼1500 K yield a vortex-antivortex pattern [26]. Single small polarons and bipolarons coexist at higher temperatures where a Drude term is found marking an insulator-metal phase transition at ∼1600 K. This electron hopping onset signals sample decomposition at still much higher temperatures.

We conclude that knowledge of the full temperature dependence of the phonon spectrum now allows us to draw similarities between *h*-$ErMnO_3$ and improper ferroelectrics that sustaining an intermediate phase become lock-in ferroelectric in a commensurate low-temperature superstructure tripling the paraelectric unit cell [91]. Inside this broader framework, pseudohexagonal K_2SeO_4, and isomorphs X_2ZnCl_4 (X = K, Rb), with a displacive and order-disorder paraelectric-incommensurate phase transition, respectively, are known prototypes. The delicate balance of long- and short-range interactions for the second-order soft mode found at T_{INC} = 129 K in K_2SeO_4 [92] is lost to a first-order order-disorder transition by isotopic replacement as in isomorph Rb_2ZnCl_4 [93], a dynamics that seems to be shared in the paraelectric to noncentrosymmetric transition of *h*-$ErMnO_3$.

In a phase that it is lattice incommensurate both, long-wavelength polarization and strain wave coexist [27] and there are interactions that tend to restore periodicity growing domains with commensurate structure and spontaneous polarizations of opposite signs separated by discommensuration regions (it conforms to a soliton regime that involves domain patterns) [94], a fact compatible with reports on polar findings in the *h*-$ErMnO_3$ intermediate phase. It is also concurrent with quasielastic x-ray-scattering lines of frozen modes

due to imperfect $(\sqrt{3} \times \sqrt{3})R30^\circ$ ordering in h-$ErMnO_3$ [50,60,95] in a picture that compounds with the dynamics imposed by the negative thermal expansion and the high temperature.

As the sample cools the soliton density diminishes, increasing the coherence of fluctuations that condensing triggers the ferroelectric phase at T_C lock-in. The result is a net macroscopic ferroelectric polarization along c. Then, the intermediate phase in h-$ErMnO_3$ may be thought of as the result of lattice instability against the creation of solitons [96,97] in a scenario for discommensurations (domain walls) [98] with latent hidden lattice symmetry [95,99–101]. Accordingly, we suggest naming h-$ErMnO_3$, $T_{INC} \sim 1500$ K, as the onset temperature for the intermediate phase that ought to be though incommensurate while the transition at Curie $T_C \sim 830$ K would signal the ferroelectric phase locking-in.

ACKNOWLEDGMENTS

N.E.M. is indebted to the laboratory on Conditions Extrêmes et Matériaux: Haute Température et Irradiation - UPR3079 CNRS (C.E.M.H.T.I.) and staff in Orléans for sharing expertise on research and for financial support in performing far-infrared reflectivity and emissivity measurements. He also thanks BESSYII at the Helmholtz-Zentrum Berlin für Materialien und Energie for beamtime allocation under Proposals No. 181-06471-ST-1.1-P and No. 172-05636-ST/R-1.1-P and for financial assistance supported by the project CALIPSOplus under Grant Agreement No. 730872 from the European Union Framework Program for Research and Innovation HORIZON 2020. J.A.A. acknowledges ILL-Grenoble for the allowed neutron time, and the financial support of the Spanish "Ministerio de Economia y Competitividad" (MINECO) through Project No. MAT2017-84496-R.

[1] P. Curie, Sur la symétrie dans les phénomènes physiques, symétrie d'un champ Électrique et d'un champ magnétique, J. Phys. Theor. Appl. **3**, 393 (1894).

[2] T. Lottermoser, T. Lonkai, U. Amann, D. Hohlwein, J. Ihringer, and M. Fiebig, Magnetic phase control by an electric field, Nature (London) **430**, 541 (2004).

[3] M. Fiebig, Th. Lottermoser, Th. Lonkai, A. V. Goltsev, and R. V. Pisarev, Magnetoelectric effects in multiferroic manganites, J. Magn. Magn. Mater. **290-291**, 883 (2005).

[4] E. F. Bertaut, F. Forrat, and P. Fang, A new class of ferroelectric: Rare earth and yttrium manganites, C. R. Acad. Sci. (Paris) **256**, 1958 (1963).

[5] H. Yakel, W. C. Koehler, E. F. Bertaut, and F. Forrat, On the crystal structure of the manganese(III) trioxides of the heavy lanthanides and yttrium, Acta Crystallogr. **16**, 957 (1963).

[6] Y. Kumagai, A. A. Belik, M. Lilienblum, N. Leo, M. Fiebig, and N. A. Spaldin, Observation of persistent centrosymmetricity in the hexagonal manganite family, Phys. Rev. B **85**, 174422 (2012).

[7] J. A. Alonso, M. J. Martínez-Lope, M. T. Casais, and M. T. Fernández-Díaz, evolution of the Jahn−Teller distortion of MnO_6 octahedra in $RMnO_3$ perovskites (R = Pr, Nd, Dy, Tb, Ho, Er, Y): A neutron diffraction study, Inorg. Chem. **39**, 917 (2000).

[8] J.-S. Zhou, J. B. Goodenough, J. M. Gallardo-Amores, E. Morán, M. A. Alario-Franco, and R. Caudillo, Hexagonal versus perovskite phase of manganite $RMnO_3$ (R = Y, Ho, Er, Tm, Yb, Lu), Phys. Rev B **74**, 014422 (2006).

[9] B. B. Van Aken, A. Meetsma, and T. T. M. Palstra, Hexagonal ErMnO, Acta Crystallogr. Sect. E: Struct. Rep. Online **57**, i38 (2001).

[10] Ph. Coeure, P. Buinet, J. C. Peuzin, G. Buisson, and E. F. Bertaut, Ferroelectric Properties of Hexagonal Orthomanganites of Yttrium and Rare Earths, in *Proceedings of the International Meeting on Ferroelectricity, Prague* (Institute of Physics of the Czechoslovak Academy of Science, Prague, 1966), Vol. 1, p. 332.

[11] R. Pauthenet and C. Veyret, Les propriétés magnétostatiques des manganites de terres rares, J. Phys. (France) **31**, 65 (1970).

[12] A. Muñoz, J. A. Alonso, M. J. Martínez-Lope, M. T. Casáis, J. L. Martínez, and M. T. Fernández-Díaz, Evolution of the magnetic structure of hexagonal $HoMnO_3$ from neutron powder diffraction data, Chem. Mater. **13**, 1497 (2001).

[13] W.C. Koehler, H- L. Yakel, E. O. Wollan, and J. B. Cable, A note on the magnetic structures of rare earth manganese oxides, Phys. Lett. **9**, 93 (1964).

[14] D. Meier, H. Ryll, K. Kiefer, B. Klemke, J.-U. Hoffmann, R. Ramesh, and M. Fiebig, Mutual induction of magnetic 3d and 4 f order in multiferroic hexagonal $ErMnO_3$, Phys. Rev. B **86**, 184415 (2012).

[15] E. F. Bertaut, M. Mercier, and R. Pauthenet, Propriétés magnétiques et structures du manganite d'yttrium, Phys. Lett. **5**, 27 (1963).

[16] J. Vermette, S. Jandl, and M. M. Gospodinov, Raman study of spin–phonon coupling in $ErMnO_3$, J. Phys.: Condens. Matter **20**, 425219 (2008).

[17] R. Basistyy, T. N. Stanislavchuk, A. A. Sirenko A. P. Litvinchuk, M. Kotelyanskii, G. L. Carr, N. Lee, X. Wang, and S.-W. Cheong, Infrared-active optical phonons and magnetic excitations in the hexagonal manganites $RMnO_3$ (R = Ho, Er, Tm, Yb, and Lu), Phys. Rev. B **90**, 024307 (2014).

[18] L. Chaix, S. de Brion, S. Petit, R. Ballou, L.-P. Regnault, J. Ollivier, J.-B. Brubach, P. Roy, J. Debray, P. Lejay, A. Cano, E. Ressouche, and V. Simonet, Magneto- to Electroactive Transmutation of Spin Waves in $ErMnO_3$, Phys. Rev. Lett. **112**, 137201 (2014).

[19] C. Standard, T. Stanislavchuk, A. A. Sirenko, N. Lee, and S.-W. Cheong, Magnons and crystal-field transitions in hexagonal $RMnO_3$ (R = Er, Tm, Yb, Lu) single crystals, Phys. Rev B **85**, 144422 (2012).

[20] N. Iwada and K. Kohn, Dielectric anomalies at magnetic transitions of hexagonal rare earth manganese oxides $RMNO_3$, J. Phys. Soc. Jpn. **67**, 3318 (1998); Magnetoelectric effect and rare earth magnetic ordering of $ErMnO_3$, Ferroelectrics **219**, 161 (1998).

[21] T. Egami, S. Ishihara, and M. Tachiki, Lattice, effect of strong electron correlation: Implication for ferroelectricity and superconductivity, Science **261**, 1307 (1993).

[22] G. Abstreiter, M. Cardona, and A. Pinczuk, in *Light Scattering in Solids IV*, edited by M. Cardona and G. Güntherodt, Topics in Applied Physics Vol. 54 (Springer-Verlag, Berlin, Heilderberg, 1984), pp. 5–150.

[23] H. G. Reik, in *Polarons in Ionic Crystals and Polar Semiconductors*, edited by J. Devreese (North-Holland, Amsterdam, 1972), p.679.

[24] P. Calvani, Optical properties of polarons, Riv. Nuovo Cimento Soc. Ital. Fis. **24**, 1 (2001).

[25] S. J. F. Byrnes, Basic theory and phenomenology of polarons, http://sjbyrnes.com/FinalPaper–Polarons.pdf.

[26] S. C. Chae, N. Lee, Y. Horibe, M. Tanimura, S. Mori, B. Gao, S. Carr, and S.-W Cheong, Direct Observation of the Proliferation of Ferroelectric Loop Domains and Vortex-Antivortex Pairs, Phys. Rev. Lett. **108**, 167603 (2012).

[27] M. Iizumi, J. D. Axe, G. Shrine, and K. K. Shimaoka, Structural phase transformation in K_2Se0_4, Phys. Rev. B **15**4392 (1977).

[28] See Supplemental Material at http://link.aps.org/supplemental/10.1103/PhysRevB.102.134305 for full description on sample preparation, experimental facilities, reflectivity (1-emissivity) fittings, and multioscillator dielectric simulation parameters.

[29] A. Muñoz, J. A. Alonso, M. J. Martínez-Lope, M. T. Casáis, J. L. Martínez, and M. T. Fernández-Díaz, Magnetic structure of hexagonal $R\mathrm{MnO_3}$ (R = Y, Sc): Thermal evolution from neutron powder diffraction data, Phys. Rev. B **62**, 9498 (2000).

[30] K. Holldack and A. J. Schnegg, THz electron paramagnetic resonance / THz spectroscopy at BESSY II, J. Large-Scale Res. Facilities **2**, A51 (2016).

[31] A. Canizarès, N. E. Massa, and J. A. Alonso (unpublished).

[32] D. De Sousa Meneses, J.-F. Brun, B. Rouseau, and P. Echegut, Polar lattice dynamics of the $MgAl_2O_4$ spinel up to the liquid state, J. Phys.: Condens. Matter **18**, 5669 (2006).

[33] L. del Campo, D. De Sousa Meneses, A. Blin, B. Rousseau, E. Véron, M. Balat-Pichelin, and P. Echegut, High-temperature radiative properties of an Yttria-Stabilized hafnia ceramic, J. Am. Ceram. Soc. **94**, 1859 (2011).

[34] M. Eckes, Opacification de matériaux oxydes au passage solide-liquide: rôle de la structure et de dynamique, Ph.D. thesis, Université d'Orléans, 2012, https://tel.archives-ouvertes.fr/tel-00838948/document.

[35] Focus Software, http://cemhti.cnrs-orleans.fr/pot/software/focus.htm.

[36] T. Kurosawa, Polarization waves in solids, J. Phys. Soc. Jpn. **16**, 1298 (1961).

[37] F. Gervais, Optical conductivity of oxides, Mater. Sci. Eng. **R39**, 29 (2002).

[38] F. Wooten, *Optical Properties of Solids* (Academic, New York, 1972).

[39] M. N. Iliev, H.-G. Lee, V. N. Popov, M. V. Abrashev, A. Hamed, R. L. Meng, and C. W. Chu, Raman- and infrared-active phonons in hexagonal $YMnO_3$: Experiment and lattice-dynamical calculations, Phys. Rev. B **56**, 2488 (1997).

[40] V. Goian, S. Kamba, C. Kadlec, D. Nuzhnyy, P. Kužel, J. Agostinho Moreira, A. Almeida, and P. B. Tavares, THz and infrared studies of multiferroic hexagonal $Y_{1-x}Eu_xMnO_3$ (x = 0 − 0.2) ceramics, Phase Transit. **83**, 931 (2010).

[41] M. Zaghrioui, V. Ta Phuoc, R. A. Souza, and M. Gervais, Polarized reflectivity and lattice dynamics calculation of multiferroic $YMnO_3$, Phys. Rev. B **78**, 184305 (2008).

[42] A. P. Litvinchuk, M. N. Iliev, V. N. Popov, and M. M. Gospodinov, Raman and infrared-active phonons in hexagonal $HoMnO_3$ single crystals: Magnetic ordering effects, J. Phys.: Condens. Matter **16**, 809 (2004).

[43] X. Wu, U. Petralanda, L. Zheng, Y. Ren, R. Hu, S-W Cheong, S. Artyukhin, and K. Lai, Low-energy structural dynamics of ferroelectric domain walls in hexagonal rare-earth manganites, Sci. Adv. **3**, e1602371 (2017).

[44] R. Milkus and A. Zaccone, Local inversion-symmetry breaking controls the boson peak in glasses and crystals, Phys. Rev. B **93**, 094204 (2016).

[45] X. Fabrèges, S. Petit, I. Mirebeau, S. Pailhès, L. Pinsard, A. Forget, M. T. Fernandez-Diaz, and F. Porcher, Spin-Lattice Coupling, Frustration, and Magnetic Order in Multiferroic $RMnO_3$, Phys. Rev. Lett. **103**, 067204 (2009).

[46] Y. Geng, N. Lee, Y. J. Choi, S.-W. Cheong, and W. Wu, Collective magnetism at multiferroic vortex domain walls, Nano Lett. **12**, 6055 (2012).

[47] T. Katsufuji, S. Mori, M. Masaki, Y. Moritomo, N. Yamamoto, and H. Takagi, Dielectric and magnetic anomalies and spin frustration in hexagonal $R\mathrm{MnO_3}$ (R = Y, Yb, and Lu), Phys. Rev. B **64**, 104419 (2001).

[48] H. A. Kramers, Théorie générale de la rotation paramagnétique dans les cristaux, Proc. Amst. Acad. **33**, 959 (1930).

[49] S. Pailhès, X. Fabrèges, L. P. Régnault, L. Pinsard-Godart, I. Mirebeau, F. Moussa, M. Hennion, and S. Petit, Hybrid goldstone modes in multiferroic $YMnO_3$ studied by polarized inelastic neutron scattering, Phys. Rev. B **79**, 134409 (2009).

[50] A. Barbour, A. Alatas, Y. Liu, C. Zhu, B. M. Leu, X. Zhang, A. Sandy, M. S. Pierce, X. Wang, S.-W. Cheong, and H. You, Partial glass isosymmetry transition in multiferroic hexagonal ErMnO3, Phys. Rev. B **93**, 054113 (2016).

[51] B. Singh, M. Vogl, S. Wurmehl, S. Aswartham, B. Büchner, and P. Kumar, Kramers doublets, phonons, crystal-field excitations, and their coupling in Nd_2ZnIrO_6, Phys. Rev. Research **2**, 023162 (2020).

[52] B. B. Van Aken, X. Fabrèges, S. Petit, J.-B. Brubach, P. Roy, M. Deutsch, A. Ivanov, L. Pinsard-Gaudart, V. Simonet, R. Ballou, and S. de Brion, Interplay between spin dynamics and crystal field in the multiferroic compound $HoMnO_3$, Phys. Rev. B **100**, 094437 (2019), and references therein.

[53] R. Migoni, H. Bilz, and D. Bäuerle, Origin of Raman Scattering and Ferroelectricity in Oxidic Perovskites, Phys. Rev. Lett. **37**, 1155 (1976).

[54] R. E. Watson, Analytic hartree-fock solutions for $O^{=}$, Phys. Rev. **111**, 1108 (1958).

[55] A. Bussmann-Holder, Electron-phonon interactions in ferroelectrics and superconductors, Ferroelectrics **150**, 25 (1993).

[56] P. Y. Yu and M. Cardona, *Fundamentals of Semiconductors*, 2nd ed. (Springer-Verlag, Berlin, 1999), Chap. III.

[57] K. Kritayakirana, P. Berger, and R. V. Jones, Optical spectra of ferroelectric-antiferromagnetic rare earth manganates, Opt. Commun. **1**, 95 (1969).

[58] G. Abstreiter, R. Trommer, M. Cardona, and A. Pinczuk, Coupled plasmon-LO phonon modes and lindhard-mermin dielectric function of n-GaAs, Solid State Commun. **30**, 703 (1979).

[59] C. Kranert, R. Schmidt-Grund, and Marius, Redshift of large wave vector LO phonon modes in wurtzite semiconductors due to the presence of free charge carriers, J. Raman Spectrosc. **46**, 167 (2015).

[60] O. Fedorova, G. Kozhina, and S. Uporov, Structural and magnetic studies of mechanically activated $ErMnO_3$, J. Alloys Compd. **740**, 677 (2018).

[61] S. Lee, A. Pirogov, J. H. Han, J.-G. Park, A. Hoshikawa, and T. Kamiyama, Direct observation of a coupling between spin, lattice and electric dipole moment in multiferroic $YMnO_3$, Phys. Rev. B **71**, 180413R (2005).

[62] G. Nénert, M. Pollet, S. Marinel, G. R. Blake, A. Meetsma, and T. T. M. Palstra, Experimental evidence for an intermediate phase in the multiferroic $YMnO_3$, J. Phys.: Condens. Matter **19**, 466212 (2007).

[63] S. M. Selbach, A. N. Løvik, K. Bergum, J. R. Tolchard, M.-A. Einarsrud, and T. Grande, Crystal Structure, Chemical expansion and phase stability of $HoMnO_3$ at high temperature, J. Solid State Chem. **196**, 528 (2012).

[64] L. Fu, M. Chao, H. Chen, X. Liu, Y. Liu, J. Yu, E. Liang, Y. Li, and X. Xiao, Negative thermal expansion property of $Er_{0.7}Sr_{0.3}NiO_{3-\delta}$, Phys. Lett. A **378**, 1909 (2014).

[65] G. D. Barrera, J. A. O. Bruno, T. H. K. Barron, and N. L. Allan, Negative thermal expansion, J. Phys.: Condens. Matter **17**, R217 (2005).

[66] W. Miller, C. W. Smith, D. S. Mackenzie, and E. Evans, Negative thermal expansion: A review, J. Mater. Sci. **44**, 5441 (2009).

[67] A. Cano, Hidden order in hexagonal $RMnO_3$ multiferroics (R = Dy–Lu, In, Y, and Sc), Phys. Rev. B **89**, 214107 (2014).

[68] V. Heine, P. R. L. Welche, and M. T. Dove, Geometrical origin and theory of negative thermal expansion in framework structures, J. Am. Ceram. Soc. **82**, 1793 (1999).

[69] N. F. Mott, The basis of the electron theory of metals, with special reference to the transition metals, Proc. Phys. Soc. London, Ser. A **62**, 416 (1949); N. F. Mott, and E. A. Davis, *Electronic Processes in Non-Crystalline Materials* (Clarendon, Oxford, 1979).

[70] A. Bari, Effects of short-range interactions on electron-charge ordering and lattice distortions in the localized state, Phys. Rev. B **3**, 2662 (1971); Superconductivity, ferroelectricity, and the mott insulator, **7**, 2128 (1973).

[71] P. Echegut, F. Gervais, and N. E. Massa, Behavior of optic phonons in the commensurate and incommensurate phases of potassium selenate, Phys. Rev. B **34**, 278 (1986).

[72] J. C. Szabo, K. Lee, V. Madhavan, and N. Trivedi, Local Spectroscopies Reveal Percolative Metal in Disordered Mott Insulators, Phys. Rev. Lett. **124**, 137402 (2020).

[73] M. E. Lines and A. M. Glass, *Principles and Applications of Ferroelectrics and Related Material* (Oxford University Press, Oxford, 2001).

[74] D. Emin, Small polarons, Phys. Today **35**(6), 34 (1982).

[75] J. T. Devreese, Polarons, arXiv:cond-mat/0004497v2.

[76] H. G. Reik and D. Heese, Frequency dependence of the electrical conductivity of small polarons for high and low temperatures, J. Phys. Chem. Solids **28**, 581 (1967).

[77] T. Holstein, Studies of polaron motion: Part II. The "small" polaron, Ann. Phys. (N.Y.) **8**, 343 (1959).

[78] R. Kubo, Statistical-mechanical theory of irreversible processes. I. General theory and simple applications to magnetic and conduction problems, J. Phys. Soc. Jpn. **12**, 570 (1957).

[79] H. G. Reik, Derivation of holstein's expression for the high temperature mobility of small polarons from kubo's formula, Phys. Lett. **5**, 236 (1963).

[80] R. Mühlstroh and H. G. Reik, Optical absorption by small polarons in p- and n-type lanthanum cobaltite, Phys. Rev. **162**, 703 (1967).

[81] H. G. Reik, Optical effects of small polarons at high frequencies with an application to rreduced strontium titanate, Z. Phys. **203**, 346 (1967).

[82] N. E. Massa, L. del Campo, D. De Sousa Meneses, P. Echegut, M. J. Martínez-Lope, and J. A. Alonso, High temperature far-infrared dynamics of orthorhombic $NdMnO_3$: Emissivity and reflectivity, J. Phys.: Condens. Matter **25**, 235603 (2013).

[83] N. E. Massa, H. Falcon, H. Salva, and R. E. Carbonio, Infrared reflectivity of the solid solutions $LaNi_{1-x}Fe_xO_3$ ($0.00 \leqslant x \leqslant 1.00$), Phys. Rev. B **56**, 10178 (1997).

[84] N. E. Massa, J. C. Dernadim, L. M. Socolovsky, M. Knobel, and X. X. Zhang, Electron dynamics in films made of transition metal nanograins embedded in SiO_2: Infrared reflectivity and nanoplasma infrared resonance, J. Appl. Phys. **105**, 114306 (2009).

[85] D. Emin, Large (bi)Polarons for novel energy conversion and superconductivity, J. Supercond. Novel Magn. **33**, 35 (2020).

[86] D. Emin, Optical properties of large and small polarons and bipolarons, Phys. Rev. B **48**, 13691 (1993).

[87] D. Emin, Pair breaking in semiclassical singlet small-bipolaron hopping, Phys. Rev. B **53**, 1260 (1996).

[88] A. Puchkov, T. Timusk, M. A. Karlow, P. D. Han, and D. A. Payne, Optical conductivity of nonmetallic $Ba_{0.69}K_{0.31}Bi0_3$ single crystals: Evidence for bipolaron formation, Phys. Rev. B **52**, R9855 (1995).

[89] N. E. Massa, L. del Campo, K. Holldack, Vinh Ta Phuoc, P. Echegut, P. Kayser, and J. A. Alonso, Far- and mid-infrared emission and reflectivity of orthorhombic and cubic $ErMnO_3$: Polarons and bipolarons, Phys. Rev. B **98**, 184302 (2018).

[90] A. Bussman-Holder and H. Büttner, Ferroelectricity in oxides, Nature (London) **360**, 541 (1992).

[91] H. Z. Cummins, Experimental studies of structurally incommensurate crystal phases, Phys. Rep. **185**, 211 (1990).

[92] N. E. Massa, F. G. Ullman, and J. R. Hardy, Interpretation of anomalies in the raman spectrum of K_2SeO_4 in terms of oxygen sublattice disorder, Phys. Rev. B **27**, 1523 (1983).

[93] N. E. Massa and V. Lemos, Intrinsic Anharmonicities in the BX_4^{-2} Orthorhombic sublattice, Phys. Rev. B **33**, 3379 (1986).

[94] D. E. Moncton, J. D. Axe, and F. J. DiSalvo, Study of Superlattice Formation in 2H-NbSe, and 2H-TaSe2 by Neutron Scattering, Phys. Rev. Lett. **34**, 734 (1975).

[95] E. M. Schmidt and R. B. Neder, Interpretation of diffuse scattering using superspace crystallography, Phys. Rev. B **100**, 054201 (2019).

[96] A. D. Bruce, The Theory of Structural Phase Transitions: Cluster Walls and Phonons, in *Solitons and Condensed Matter Physics*, edited by A. R. Bishop and T. Schneider (Springer-Verlag, Berlin, 1978), p. 116.

[97] A. D. Bruce, R. A. Cowley, and A. F. Murray, The theory of structurally incommensurate systems. II. commensurate-incommensurate phase transitions, J. Phys. C **11**, 3591 (1978).

[98] W. L. McMillan, Theory of discommensurations and the commensurate-incommensurate charge-density-wave phase transition, Phys. Rev. B **14**, 1496 (1976).

[99] P. M. de Wolff, Symmetry operations for displacively modulated structures, Acta Crystallogr., Sect. A **33**, 493 (1977).

[100] T. Janssen and A. Janner, Aperiodic crystals and superspace concepts, Acta Crystallogr., Sect. B **70**, 617 (2014).

[101] A. Janner and T. Janssen, Symmetry of periodically distorted crystals, Phys. Rev. B **15**, 643 (1977); Symmetry of incommensurate crystal phases. I. commensurate basic structures, Acta Crystallogr., Sect. A **36**, 399 (1980).